RSC Advances

PAPER

View Article Online
View Journal | View Issue

Cite this: *RSC Adv.*, 2025, **15**, 2152

Mass production of ultrasmall Mn_3O_4 nanoparticles for glutathione responsive off-on T_1/T_2 switching magnetic resonance imaging and tumor theranostics

Qinghua Xie,[ae] Gaorui Zhang,[bc] Dawei Zhou,[bc] Hong Liu,[ad] Dexin Yu *[bc] and Jiazhi Duan *[ad]

Received 8th October 2024
Accepted 18th December 2024

DOI: 10.1039/d4ra07224c

rsc.li/rsc-advances

Individual theranostics with an integrated multifunction holds considerable promise for clinical application compared with multicomponent regimes. Mn_3O_4 nanoparticles with an ultrasmall size (4 nm) and mass production capability were developed with dual function of integrated tumor magnetic resonance imaging (MRI) and therapy. The high valence state of Mn_3O_4 nanocrystals enables a sensitive reaction with the glutathione (GSH) molecule and favorable decomposition ability, which further induces a unique, favorable, variable T_1 turn-off and T_2 turn-on MRI property. In addition, ultrasmall Mn_3O_4 nanoparticles reacted with high-level GSH in the tumor microenvironment induces responsive and enhanced variable T_1- and T_2-MRI imaging capability for accurate cancer diagnosis. Moreover, the synthesized ultrasmall Mn_3O_4 nanoparticles exhibit considerable ferroptosis effect towards tumor cells and excellent *in vivo* biocompatibility, thus indicating promising effective cancer treatment application. The developed ultrasmall Mn_3O_4 nanoparticles with integrated dual functions of GSH-responsive variable T_1 and T_2 MRI imaging effects and ferroptosis capability show promising potential as a candidate for tumor theranostics in clinical applications.

1. Introduction

The current epidemiology of cancer shows that the incidence rate and mortality rate of cancer are increasing annually.[1,2] The accurate diagnosis of cancer, especially in the early stage, is of great importance for its treatment.[3] Among the various diagnostic techniques, MRI has been recognized as one of the most powerful medical diagnostic tools with comprehensive and detailed detection ability in the clinic.[4,5] MRI is proposed as an effective noninvasive method with high spatial resolution and real-time monitoring capability, which can reflect whole tumor biological features and account for accurate diagnosis and treatment.[6,7] In addition, numerous recent preclinical studies report that the combination of MRI detection and tumor therapy holds great promise for enhancing both cancer treatment efficiency and effectiveness.[8–10] Although MRI tests possess huge advantages, their sensitivity and resolution ratio for differentiating various diseases in some cases remains to be improved using a well-designed contrast agent.[11,12] Therefore, developing advanced MRI contrast agents integrated with high cytotoxicity towards tumor cells has become one of the most urgent tasks for improving the efficiency of synergistic MRI diagnosis and cancer treatment.[13–15]

Manganese-based nanomaterials, a hot research target in recent years, have aroused considerable interest from researchers owing to their unique characteristic and broad application in biology and medicine, especially for tumor MRI theranostics.[16–18] According to the MRI principle, MRI contrast agents are generally classified into two types: positive and negative signal improvements, which are T_1- and T_2-weighted MRI, respectively.[19,20] Moreover, the integration of T_1- and T_2-mode MRI in one operation in the clinic could immensely promote diagnosis accuracy and efficiency.[21] Previous research has shown that Mn-based nanomaterials including MnO, Mn_3O_4 and MnO_2 possess an ideal T_1-mode MRI enhancement ability, thus enabling the development of a competitive alternative contrast agent.[22–24] Nevertheless, the development strategy for Mn-based nanomaterials for T_1 and T_2 dual-mode MRI mainly relies on combination with the T_2 MRI contrast agent of Fe_3O_4, which requires a rigorous process and extensive work. The translation of an Mn-based T_1 and T_2 dual-mode MRI

[a]State Key Laboratory of Crystal Materials, Shandong University, Jinan, Shandong, 250100, P.R. China. E-mail: jiazhiduan_sdu@163.com
[b]Department of Radiology, Qilu Hospital of Shandong University, Jinan, Shandong, 250012, China. E-mail: yudexin0330@sina.com
[c]Translational Medicine Research Center in Nano Molecular and Functional Imaging of Shandong University, Jinan, 250100, China
[d]Institute for Advanced Interdisciplinary Research, University of Jinan, Jinan 250022, P. R. China
[e]Shandong BIOBASE Biology Co., Ltd, China

agent to clinical application is challenging as there exist many obstacles that need to be overcome, including scaling up the production, improving stability and exporting the standard.[25] Furthermore, Mn-based nanomaterials have been utilized for tumor treatment for their effective antitumor effect, negligible immunogenicity, and excellent MRI contrast enhancement.[26,27] The tumor microenvironment is usually characterized by a high level of glutathione (GSH) and H_2O_2. Based on these features, the development of Mn-based nanomaterials as tumor microenvironment responsive nanoagents for both tumor T_1/T_2 MRI and therapy can help enhance cancer treatment and promote their clinical translation.[28,29]

Herein, we well designed advanced theranostic ultrasmall Mn_3O_4 nanoparticles that possess tumor microenvironment responsive off-on T_1/T_2 switching MRI imaging capability and an effective ferroptosis therapy effect. The synthesized ultrasmall Mn_3O_4 nanoparticles are about 4 nm in size with excellent uniformity and mass production ability. The high valence state Mn in Mn_3O_4 nanocrystals offer the effective glutathione (GSH) responsive ability and variable MRI imaging property. The sensitive reaction of ultrasmall Mn_3O_4 nanoparticles with a GSH molecule enable the functional T_1 turn-off to T_2 turn-on MRI switching effect, which furnish better signal quality and diagnose accuracy in an *in vitro* and *in vivo* environment. Moreover, ultrasmall Mn_3O_4 nanoparticles could effectively induce the ferroptosis effect to tumor cells with favorable *in vivo* biocompatibility. The finely developed individual ultrasmall Mn_3O_4 nanoparticles with an integrated responsive MRI effect and ferroptosis function make it an ideal candidate for tumor theranostics in the clinic.

2. Experimental methods

2.1 Mass production and modification of ultrasmall Mn_3O_4 nanoparticles

Oleylamine, oleyl alcohol, dimercaptosuccinic acid (DMSA), manganese(II) acetate tetrahydrate and anhydrous sodium carbonate were purchased from Shanghai Macklin Biochemical Co. Ltd Ethanol, tetrahydrofuran and *n*-hexane were purchased from Sinopharm Chemical Reagent Co. Ltd

Ultrasmall Mn_3O_4 nanoparticles were synthesized according to previous research with some modifications.[30] Briefly, 60 g oleylamine, 100 g oleyl alcohol and 300 mL 1-octadecene were mixed with 4.9 g manganese(II) acetate tetrahydrate. The mixture was then homogenized and slowly heated to 100 °C. Thereafter, 2 mL manganese acetate tetrahydrate aqueous (0.1 M) was added to the solution. The reaction was maintained for 30 min and then cooled to room temperature. Mn_3O_4 nanoparticles were obtained by adequately washing the solution with ethanol and *n*-hexane.

Ultrasmall Mn_3O_4 nanoparticles were modified with the DMSA molecule to endow better dispersity in water. Briefly, 10 mg of the obtained Mn_3O_4 nanoparticles were added to 1 mL tetrahydrofuran, and 10 mg DMSA was added to 1 mL anhydrous sodium carbonate aqueous. The two solutions were well mixed and applied for ultrasonic treatment for 30 min. Mn_3O_4-DMSA was purified *via* centrifugation and the freeze-drying process.

2.2 Characterization

The size and morphology of the synthesized nanomaterials were detected using TEM and HRTEM (JEM-2100, JEOL, Tokyo, Japan). The structure information of the nanomaterials was tested using XRD (D8 Advance, Bruker, Ettlingen, Germany). The atomic valence and element composition information were characterized through XPS. FTIR spectroscopy (Nicolet Nexus 670, Thermo Fisher Scientific, Inc., Waltham, MA) was used to characterize the functional group of nanomaterials. Size distribution and zeta potential value were tested using a Malvern Zetasizer Nano Series. The absorbance spectrum of nanomaterials was characterized using a UV–vis spectrophotometer (UV-6100, Meipuda, Xi'an, China). The MRI property was tested using a 3.0-T clinical MRI scanner (GE Signa HDx 3.0 T MRI, USA) in a 16-channel brain coil.

2.3 Cells and animals

Mouse 4T1 cells were obtained from the Institute of Biochemistry and Cell Biology (Shanghai, China). Experiment mice (BALB/c, male) were acquired from Jinan Peng Yue Laboratory Animal Co., Ltd, Jinan, China. The 4T1 cells and mice were cultured as per manufacturer instructions. All mouse research has the approbation of Laboratory Animal Ethical and Welfare Committee of Shandong University, Cheeloo College of Medicine, China (accreditation number: SYXK:20190005) and was performed in line with the guidelines.

The subcutaneous tumor-bearing model was constructed by injecting 1×10^6 4T1 cells in the right hind leg of BALB/c male mice (6–8 week-old). The liver metastatic tumor model was constructed by injecting 5×10^4 4T1 cells in 2 mL normal saline into the tail vein of mice.

2.4 MRI property measurement

The T_1 and T_2 MRI imaging and relaxivity property of ultrasmall Mn_3O_4 nanoparticles (6.25, 12.5, 25, 50, 100, and 200 μg mL^{-1}) were tested using a 3.0-T MR scanner. Furthermore, 5 mM and 10 mM GSH were reacted with ultrasmall Mn_3O_4 nanoparticles (6.25, 12.5, 25, 50, 100, and 200 μg mL^{-1}), and MRI imaging and relaxivity were recorded using the same method. The T_1 and T_2 MRI imaging abilities of ultrasmall Mn_3O_4 nanoparticles for cancer cells (4T1) were assessed by incubating 4T1 cells with 50 μg mL^{-1} Mn_3O_4 nanoparticles for 2 h, 4 h, 8 h, and 12 h. The treated 4T1 cells were resuspended in 1 mL of the cell culture medium and characterized using an MRI scanner.

The *in vivo* MRI imaging effect of ultrasmall Mn_3O_4 nanoparticles was verified in both the 4T1 subcutaneous tumor and liver metastatic tumor models. The tumor-bearing mouse was treated with 5 mg kg^{-1} ultrasmall Mn_3O_4 nanoparticles through intravenous injection and then examined using an MRI scanner; the obtained images and signal intensity were recorded at the time points of 0, 2 and 4 h.

2.5 Cell viability assay of ultrasmall Mn_3O_4 nanoparticles

The cell viability of ultrasmall Mn_3O_4 nanoparticles was tested using live/dead staining. 4T1 cells were cocultured with Mn_3O_4

nanoparticles (6.25, 12.5, 25, and 50 μg mL^{-1}) for 24 h and then stained with a live/dead regent, and the cells were observed using an inverted fluorescence microscope. The cytotoxicity of ultrasmall Mn_3O_4 nanoparticles was assayed using CCK-8 and flow cytometry, and 4T1 cells were cocultured with Mn_3O_4 nanoparticles (6.25, 12.5, and 25 μg mL^{-1}) for 24 h and then detected using a CCK-8 kit as well as counting the live and dead cells using flow cytometry. The cleaved caspase-3 level in 4T1 cells after incubation with Mn_3O_4 nanoparticles (6.25, 12.5, and 25 μg mL^{-1}) for 24 h was measured using western blot analysis.

2.6 Ferroptosis therapy measurement

The 4T1 cells were cocultured with Mn_3O_4 nanoparticles (6.25, 12.5, and 25 μg mL^{-1}) for 24 h and stained using a ferroptosis marker. Dichlorofluorescein diacetate (DCFH-DA, 10 μM) was utilized to detect the intracellular ROS level *via* incubation with the 4T1 cells for 20 min. The lipid ROS sensor C11 $BODIPY^{581/591}$ (8 μM) was used to assess the lipid peroxidation level in 4T1 cells, and the treated cells were observed using fluorescence microscopy. The GPX4 level in 4T1 cells after incubation with Mn_3O_4 nanoparticles was measured using western blot analysis.

2.7 Biosafety evaluation

The *in vivo* biocompatibility of Mn_3O_4 nanoparticles was assayed before additional MRI and treatment application. The hemolytic property of Mn_3O_4 nanoparticles (6.25, 12.5, 25, 50, and 100 μg mL^{-1}, experiment group) was tested by comparing the hemolysis rate in the group of isolated red blood cells and the group treated with PBS (positive control) and pure water (negative control). The primary organs of mice after injection with Mn_3O_4 nanoparticles for 24 h were stained with hematoxylin-eosin (HE), and tissue slicing was observed using fluorescence microscopy.

2.8 Statistical analysis

The data were shown as the average ± standard deviation. Comparison between two group statistics was performed using Student's *t*-test. Comparison in different group statistics was used with the analysis of variance, and the data were defined with $^{*}p < 0.05$, $^{**}p < 0.01$ and $^{***}p < 0.001$.

3. Results and discussion

3.1 Synthesis and characterizations of ultrasmall Mn_3O_4 nanoparticles

Fig. 1a shows the mass production procedure scheme of ultrasmall Mn_3O_4 nanoparticles. The size and morphology of the synthesized Mn_3O_4 nanoparticles were characterized using TEM (Fig. 1b). The TEM result shows that the Mn_3O_4 nanoparticles are about 4 nm with an ultrasmall size and uniform shape. The enlarged HRTEM image (Fig. 1c) indicates that the obtained ultrasmall Mn_3O_4 nanoparticles are of good crystallinity. After modification with the DMSA molecule, the Mn_3O_4

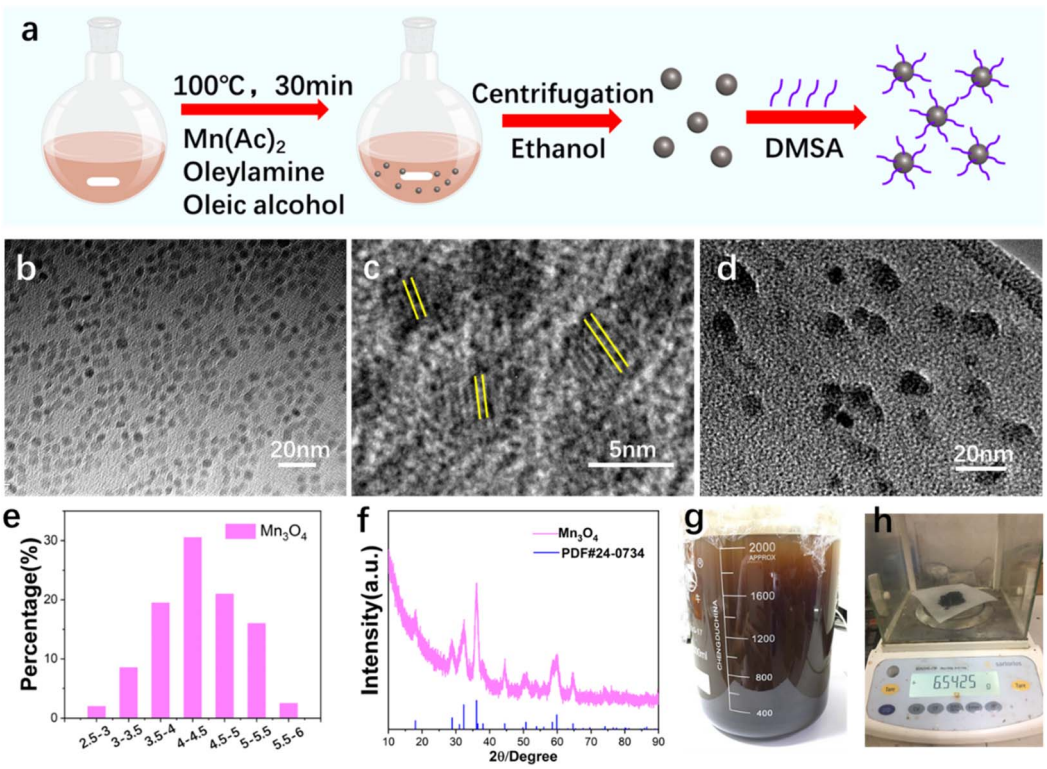

Fig. 1 Synthesis and characterization of ultrasmall Mn_3O_4 nanoparticles. (a) The synthesis scheme of ultrasmall Mn_3O_4 nanoparticles. (b) TEM, (c) HRTEM image of ultrasmall Mn_3O_4 nanoparticles. (d) HRTEM image of Mn_3O_4-DMSA nanoparticles. (e) Size distribution statistic and (f) XRD pattern of ultrasmall Mn_3O_4 nanoparticles. (g) Washing procedure and (h) mass production of ultrasmall Mn_3O_4 nanoparticles.

nanoparticles retain their original size and morphology (Fig. 1d). The size distribution statistic of ultrasmall Mn_3O_4 nanoparticles was analyzed (Fig. 1e), and the result indicates that the size is around 2–6 nm, and the main size is about 4.5 nm. The XRD pattern (Fig. 1f) of the synthesized nanoparticles confirms that nanoparticles are of excellent crystallinity and correspond to the pure Mn_3O_4 phase (standard PDF card: 24-0734). The washing procedure (Fig. 1g) and final production of 6.54 g of ultrasmall Mn_3O_4 nanoparticles (Fig. 1h) confirm their large-scale production and clinical translation potential.

The DMSA molecule modification endows ultrasmall Mn_3O_4 nanoparticles with better dispersity, which is essential for their bioapplications. XPS was utilized to analyze the Mn valence state of Mn_3O_4 (Fig. 2a) and Mn_3O_4-DMSA (Fig. 2b). XPS spectrum results confirm the existence of Mn^{2+} and Mn^{3+} in Mn_3O_4 and Mn_3O_4-DMSA, which agrees with the element composition. The DMSA molecule modification of Mn_3O_4 was further studied using the FTIR spectrum (Fig. 2c). The absorption peaks of Mn_3O_4 located at 2981.7 and 2849.6 cm^{-1} correspond to N–H bond stretching vibration, which indicates the existence of the residual oleylamine molecule. For Mn_3O_4-DMSA, the peaks of N–H vibration disappeared, suggesting the successful substitution of the DMSA molecule with the oleylamine molecule on the surface of Mn_3O_4 nanoparticles. The synthesized Mn_3O_4-DMSA nanoparticles show excellent dispersity in water (Fig. 2d, inside) and intense absorbance around 300–600 cm^{-1} (Fig. 2d). The hydrated particle size (%number) of Mn_3O_4-DMSA in PBS (Fig. 2e) shows a normal distribution for 10–50 nm and is mainly located at 20 nm, which is beneficial for its utilization as a bioagent *in vivo*. The zeta potential values of Mn_3O_4-DMSA in PBS (pH = 7, pH = 6.5 and pH = 5.5) are as high as -41.7 ± 6.9 mV, -23.3 ± 4.57 mV and -28 ± 4.51 mV (Fig. 2f), indicating the nanoparticles are of excellent dispersity and stability in aqueous PBS. The size distribution (%intensity) of Mn_3O_4-DMSA in PBS in Fig. 2g reveals that most Mn_3O_4 nanoparticles are monodispersed and there are few aggerates in the aqueous solution. The size distribution (%number) of Mn_3O_4-DMSA after long-term stability placement (2 weeks) in PBS (Fig. 2h) and PBS + BSA (Fig. 2i) conditions shows similar distribution tendency with small size differences. The hydrated particle size distribution and zeta potential values of Mn_3O_4-DMSA in different conditions demonstrate its promising bioapplication *in vivo*.

The MRI imaging property of Mn_3O_4 nanoparticles *in vitro* was researched in detail. As shown in Fig. 3a, the phantom

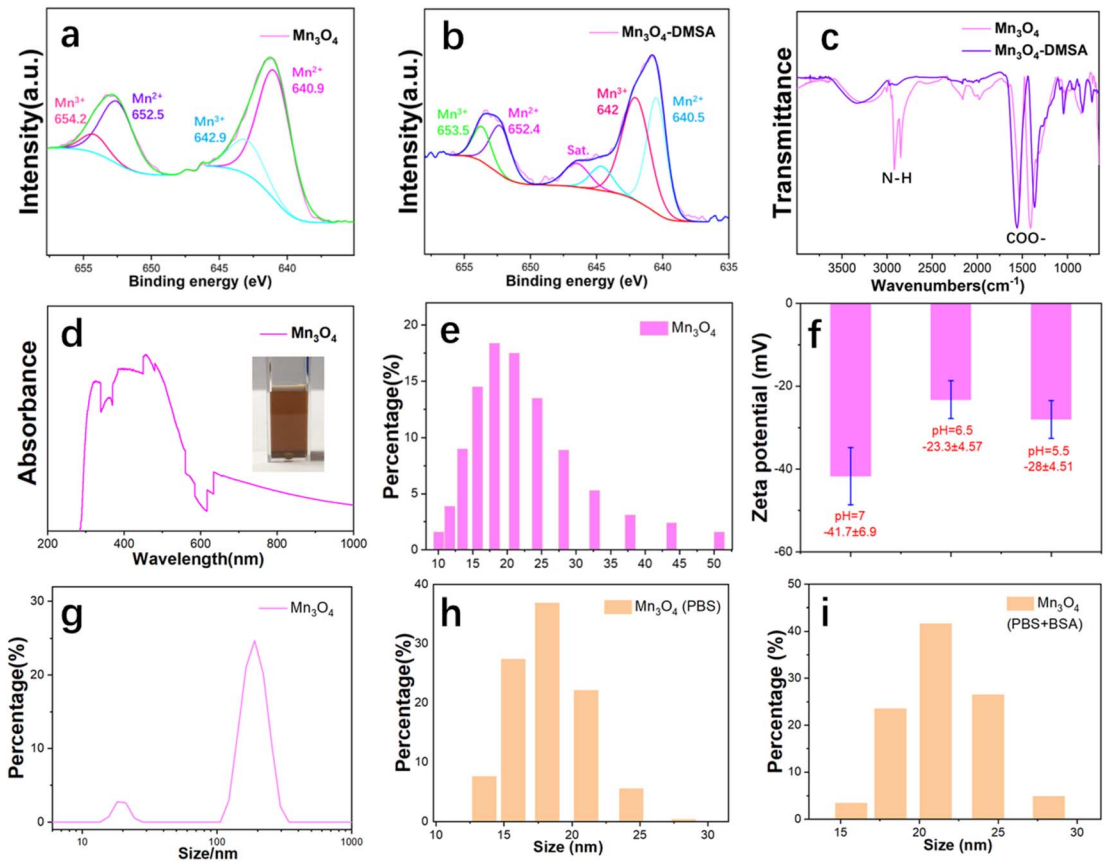

Fig. 2 Characterization of ultrasmall Mn_3O_4 and Mn_3O_4-DMSA nanoparticles. (a) XPS pattern of ultrasmall Mn_3O_4 nanoparticles. (b) XPS pattern of Mn_3O_4-DMSA nanoparticles. (c) FTIR pattern of Mn_3O_4 and Mn_3O_4-DMSA nanoparticles. (d) UV-vis absorbance of Mn_3O_4-DMSA aqueous and the real image in water (inset). (e) Size distribution (%number) of Mn_3O_4-DMSA in PBS. (f) Zeta potential values of Mn_3O_4-DMSA in PBS with different pH. (g) Size distribution (%intensity) of Mn_3O_4-DMSA in PBS. Size distribution (%number) of Mn_3O_4-DMSA after long-term stability placement (2 weeks) in (h) PBS and (i) PBS + BSA condition.

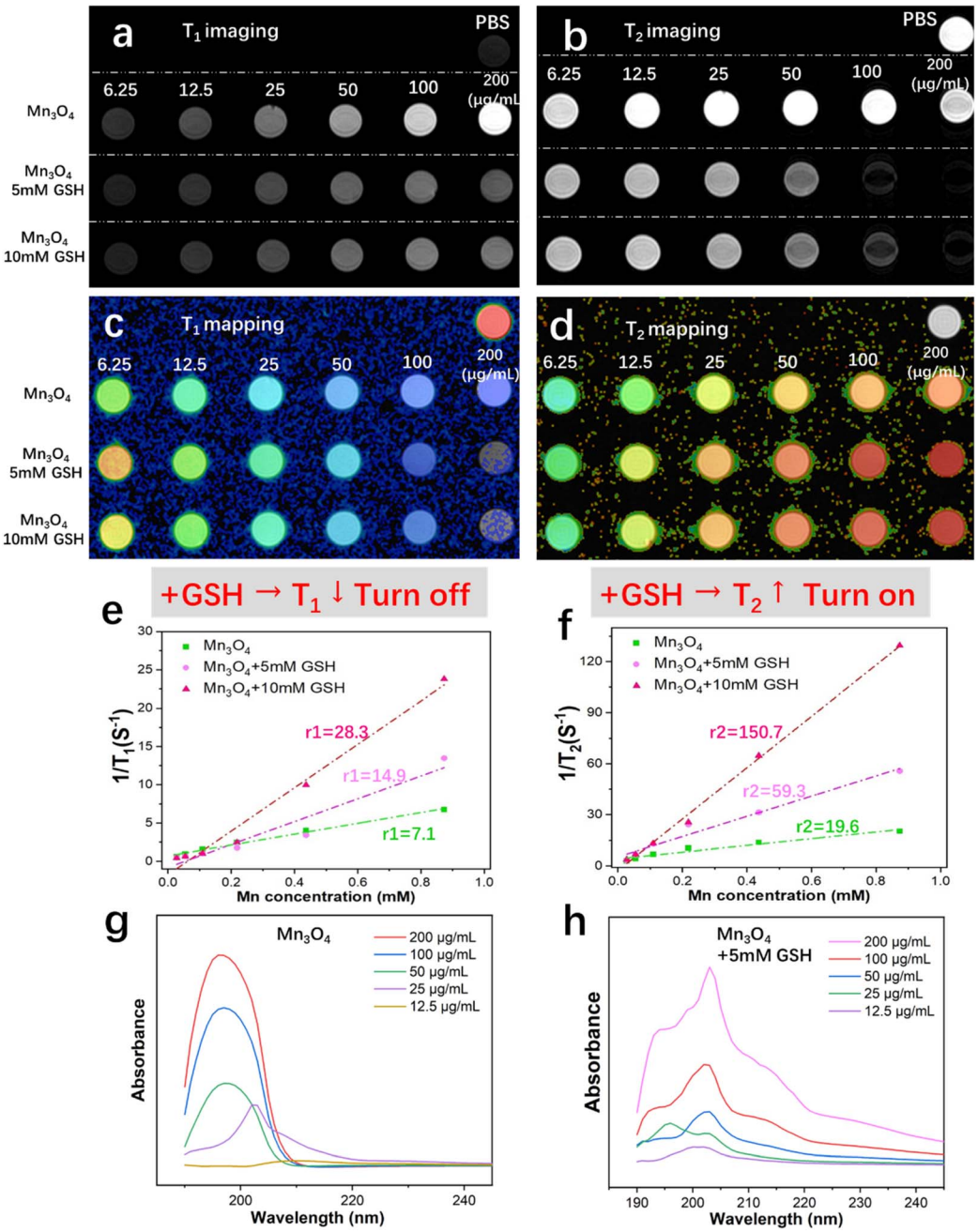

Fig. 3 GSH-responsive MRI variation measurement. (a) T_1 and (b) T_2 MRI imaging of Mn_3O_4 (6.25, 12.5, 25, 50, 100, and 200 μg mL^{-1}) as well as the MRI image after reaction with 5 mM and 10 mM GSH. (c) T_1 and (d) T_2 MRI mapping image of Mn_3O_4 (6.25, 12.5, 25, 50, 100, and 200 μg mL^{-1}) as well as the MRI mapping image after reaction with 5 mM and 10 mM GSH. (e) The r_1 and (f) r_2 values of Mn_3O_4 after reaction with 0, 5 and 10 mM GSH. (g) UV-vis absorbance of a gratitude concentration of Mn_3O_4. (h) UV-vis absorbance of gratitude concentration Mn_3O_4 after reaction with 5 mM GSH.

image of T_1-weighted imaging shows an obvious increased lightness as the concentration of Mn_3O_4 increased from 6.25 to 200 μg mL^{-1}, presenting a typical T_1 MRI imaging characteristic. When Mn_3O_4 was reacted with 5 mM GSH, the phantom image lightness shows a slight increased tendency with increasing concentration and darker intensity compared with the untreated group (pure Mn_3O_4). As the treatment concentration of GSH increased to 10 mM, the phantom image lightness becomes darker and weaker compared with the treatment of 5 mM GSH, showing a GSH-responsive T_1 turn-off effect. The phantom image of T_2-weighted imaging is shown in Fig. 3b. The results show that pure Mn_3O_4 has almost no T_2 weight-imaging effect, indicating that Mn_3O_4 is an effective and pure T_1 MRI contrast agent and the state of T_2 MRI imaging is off. After treatment with 5 mM and 10 mM, the darkness of T_2 imaging becomes deeper as the concentration of GSH increased, indicating a sensitive GSH responsive T_2 turn-on property. To summarize, ultrasmall Mn_3O_4 nanoparticles possess a unique

and favorable GSH responsive capability of T_1 turn-off and T_2 turn-on the MRI switching effect.

The T_1 and T_2 relaxation times of Mn_3O_4 nanoparticles treated with the gradient concentration of GSH were measured, and the results were shown as T_1 and T_2 mapping (Fig. 3c and d). The corresponding r_1 and r_2 relaxivity values of T_1 and T_2 relaxation times were calculated from the plots of relaxation time *versus* Mn_3O_4 concentration (Fig. 3e and f). The r_1 value of T_1 MRI imaging in the Mn_3O_4 group (6.25–200 μg mL^{-1}) is 7.1 mM^{-1} s^{-1}; with the reaction of 5 mM and 10 mM GSH, the r_1 values increase to 14.9 and 28.3 mM^{-1} s^{-1}, respectively. The r_2 value of T_2 MRI imaging for the Mn_3O_4 group (6.25 to 200 μg mL^{-1}) is 19.6 mM^{-1} s^{-1}; after treatment with 5 mM and 10 mM GSH, r_2 values increase to 59.3 and 150.7 mM^{-1} s^{-1}, respectively. The T_1 and T_2 MRI mapping and relaxivity values indicate the GSH-responsive T_1 turn-off and T_2 turn-on property. As Mn_3O_4 nanoparticles show a brown color and possess obvious light absorption, the UV-vis absorbance spectrum of Mn_3O_4 nanoparticles at different concentrations (12.5–200 μg mL^{-1}) was obtained (Fig. 3g). Absorption intensity during 180–200 nm increases with an increasing in Mn_3O_4 concentration. Fig. 3h shows the UV-vis absorbance spectrum of Mn_3O_4 nanoparticles at different concentrations (12.5–200 μg mL^{-1}) after reaction with 5 mM GSH. These results confirm the intense reaction between Mn_3O_4 nanoparticles and the GSH molecule as well as MRI variation evidence.

3.2 Cell viability and ferroptosis therapy of ultrasmall Mn_3O_4 nanoparticles

Before ultrasmall Mn_3O_4 nanoparticles were used as nanomedicine *in vivo*, their cell viability was assessed. The living/dead staining images of 4T1 cells incubated with 6.25, 12.5, 25 and 50 μg mL^{-1} Mn_3O_4 are shown in Fig. 4a. As the

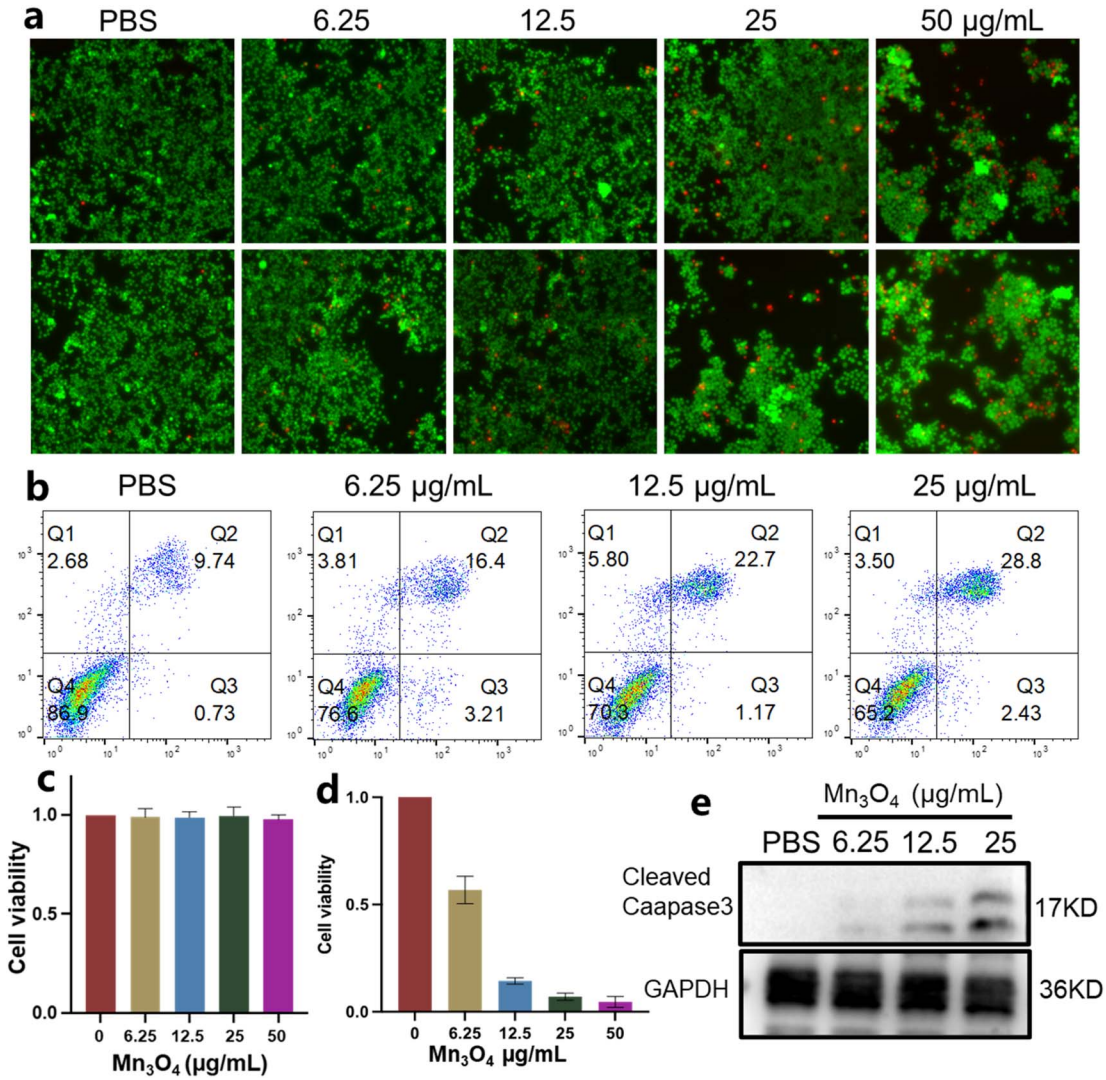

Fig. 4 Cell viability test of ultrasmall Mn_3O_4 nanoparticles. (a) Living/dead staining of 4T1 cells after incubation with Mn_3O_4 (6.25, 12.5, 25, and 50 μg mL^{-1}). (b) Flow cytometry assay of 4T1 cells after coculture with Mn_3O_4 (6.25, 12.5, and 25 μg mL^{-1}). (c) CCK-8 test for endothelial cells after treating with Mn_3O_4 (6.25, 12.5, 25, and 50 μg mL^{-1}). (d) CCK-8 test for 4T1 cells after treating with Mn_3O_4 (6.25, 12.5, 25, and 50 μg mL^{-1}). (e) The cleaved caspase-3 express level in 4T1 cells after treating with Mn_3O_4 (6.25, 12.5, and 25 μg mL^{-1}).

concentration of Mn_3O_4 nanoparticles increase, the numbers of living 4T1 cells decrease and that of the dead cells obviously increase, showing an outstanding antitumor effect. The treated 4T1 cells were analyzed using flow cytometry, and the results are shown in Fig. 4b, which confirms the good antitumor effect of Mn_3O_4 nanoparticles. The CCK-8 test was utilized to evaluate the biocompatibility of ultrasmall Mn_3O_4 nanoparticles (Fig. 4c and d). With an increase in Mn_3O_4 concentration, the cell viability of endothelial cells remains unchanged, but the cell viability of 4T1 cells dramatically decreases, indicating the excellent biocompatibility of ultrasmall Mn_3O_4 nanoparticles with normal cells and distinct growth inhibition and a toxicity effect towards tumor cells. Cleaved caspase-3 is the typical marker of apoptosis, and the expression level of cleaved caspase-3 indicates the associated apoptosis state of cells. As shown in Fig. 4e, the treatment of Mn_3O_4 nanoparticles could induce elevated expression of cleaved caspase-3, and the expression level was promoted by increased Mn_3O_4 concentration. The cell viability assays confirm that ultrasmall Mn_3O_4 nanoparticles possess obvious cytotoxicity toward tumor cells and an intense antitumor effect.

To classify the ferroptosis antitumor mechanism of ultrasmall Mn_3O_4 nanoparticles, the ROS staining of 4T1 cells treated with Mn_3O_4 (6.25, 12.5, and 25 μg mL^{-1}) was performed, and the results are shown in Fig. 5a. The corresponding relative fluorescence intensity is shown in Fig. 5c. The ROS level in 4T1 cells after treatment with ultrasmall Mn_3O_4 nanoparticles is considerably promoted, and the promotion degree rises with the increasing of Mn_3O_4 concentration. The ultrasmall Mn_3O_4 nanoparticles could react with GSH and H_2O_2. Therefore, the increased ROS level is induced using the GSH consumption ability and Fenton-like reaction between ultrasmall Mn_3O_4 nanoparticles and the high level of intracellular H_2O_2. For the ferroptosis pathway, the elevated ROS level could induce lipid peroxidation in tumor cells. Therefore, the BODIPY 581/591 C11 of the lipid peroxidation sensor was applied to detect the lipid status in 4T1 cells. The staining result is shown in Fig. 5b, and the corresponding relative fluorescence intensity is shown in Fig. 5d. These statistical data indicate that the ultrasmall Mn_3O_4 nanoparticles enhance lipid peroxidation in tumor cells. GPX4 in tumor cells could effectively decrease the ROS and lipid peroxidation levels, which could be considered an important marker of ferroptosis. The GPX4 expression level in 4T1 tumor cells after incubation with ultrasmall Mn_3O_4 nanoparticles (6.25, 12.5, and 25 μg mL^{-1}) is shown in Fig. 5e. With an increase in Mn_3O_4 concentration, the GPX4 expression level

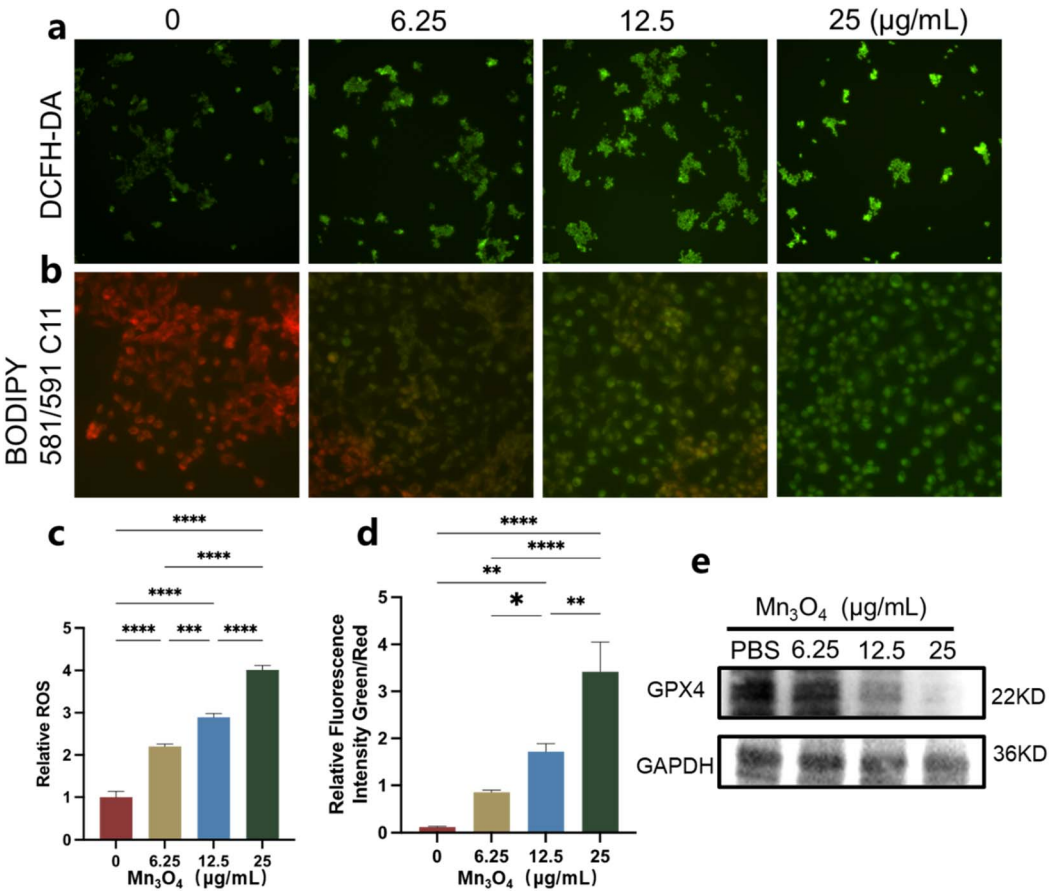

Fig. 5 Ferroptosis therapy of ultrasmall Mn_3O_4 nanoparticles. (a) ROS staining of 4T1 cells after treating with Mn_3O_4 (6.25, 12.5, and 25 μg mL^{-1}) and (c) corresponding relative fluorescence intensity. (b) Lipid peroxidation staining of 4T1 cells after treating with Mn_3O_4 (6.25, 12.5, and 25 μg mL^{-1}) and (d) corresponding relative fluorescence intensity comparison. (e) GPX4 expression level in 4T1 cells after incubation with Mn_3O_4 (6.25, 12.5, and 25 μg mL^{-1}) assessed using western blot analysis.

remarkedly decreases, which is induced by an increased ROS level and reduced GSH concentration. These results confirm the efficient ferroptosis antitumor effect of ultrasmall Mn_3O_4 nanoparticles.

3.3 T_1 and T_2 MRI signal variation for ultrasmall Mn_3O_4 nanoparticles *in vivo*

The MRI imaging of 4T1 tumors both *in vitro* and *in vivo* using ultrasmall Mn_3O_4 nanoparticles was characterized in detail. The T_1 and T_2 MRI imaging properties of 4T1 cells *in vitro* are shown in Fig. 6a and b. After incubation of 4T1 cells with Mn_3O_4 nanoparticles for 2, 4, 8 and 12 h, the lightness intensity of T_1 MRI image, as shown in Fig. 6a, gradually elevates with increase in incubation time, which is due to the enhanced accumulation of Mn_3O_4 nanoparticles in 4T1 tumor cells. The darkness of the T_2 MRI image in Fig. 6b is distinctly promoted together with the incubation time scale, which could be caused by the reaction with high-level GSH in 4T1 cells. The MRI imaging of ultrasmall Mn_3O_4 nanoparticles for 4T1 tumor cells identified T_1 and T_2 MRI variation at the cellular level. The ultrasmall Mn_3O_4

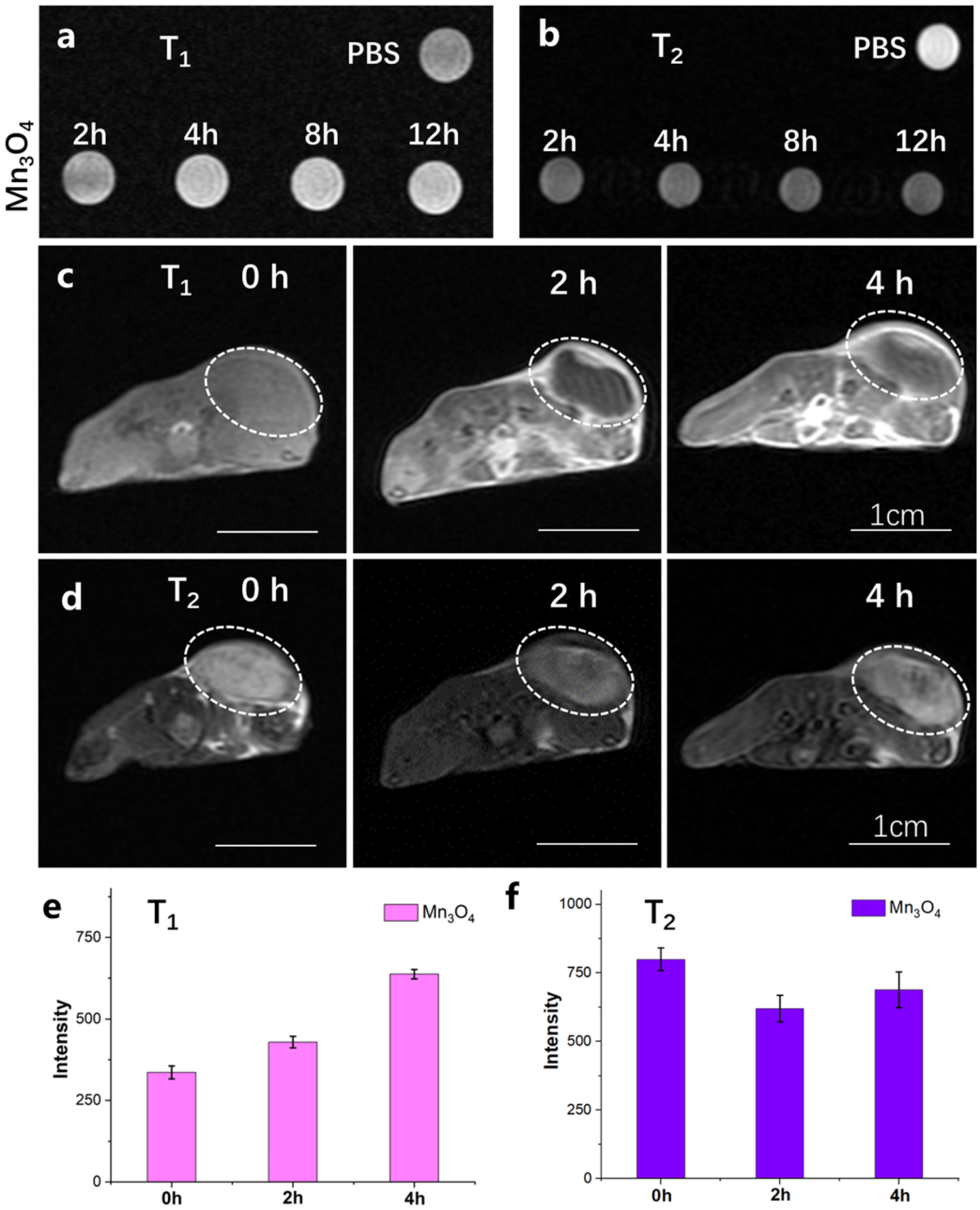

Fig. 6 T_1 and T_2 MRI signal variation of ultrasmall Mn_3O_4 nanoparticles in 4T1 cells and subcutaneous tumors. (a) T_1 and (b) T_2 MRI imaging and signal variation of 4T1 cells after incubation with Mn_3O_4 for 2, 4, 8 and 12 h. (c) T_1 and (d) T_2 MRI imaging and signal variation of the subcutaneous tumor after injection with Mn_3O_4 (5 mg kg^{-1}) for 0, 2 and 4 h. (e) The corresponding T_1 and (f) T_2 MRI imaging signal intensity variation of the subcutaneous tumor.

nanoparticles for *in vivo* tumor MRI imaging were then detected in the 4T1 subcutaneous tumor. The T_1 and T_2 MRI imaging and signal variation results of tumors after intravenous injection of Mn_3O_4 (5 mg kg^{-1}) for 0, 2 and 4 h are shown in Fig. 6c and d, respectively. The corresponding T_1 and T_2 MRI imaging signal intensity variations are shown in Fig. 6e and f, respectively. After the treatment of Mn_3O_4 for 2 h and 4 h, the T_1 signal intensity increases to 127.6% and 189.6%, respectively, compared with the control group, indicating the effectively enhanced T_1 MRI imaging ability. In addition, the T_2 signal intensity decreases to 77.5% and 86.1%, respectively, compared with the control group, showing a promoted T_2 MRI imaging effect, which could be induced by the high level of GSH in the tumor microenvironment. The *in vitro* tumor microenvironment mimic condition (5 and 10 mM GSH in Fig. 3) is static without a continued blood flow. After the tail vein injection of Mn_3O_4, Mn_3O_4 gradually accumulated in the tumor site and induced the T_1 MRI effect. Furthermore, GSH in the tumor environment induced the T_1 turn-off and T_2 turn-on effect. The cooperative results endow both the T_1 turn-on and T_2 turn-on effects. In the *in vitro* mimic condition, no Mn_3O_4 accumulation process occurs, which directly induces the T_1 turn-off and T_2 turn-on effects. The MRI imaging results of tumors both *in vitro* and *in vivo* collaboratively illustrate the variable T_1 and T_2 MRI imaging capability of ultrasmall Mn_3O_4 nanoparticles.

Tumor metastasis is the main reason of recurrence and low cure rate of cancer. To excavate the MRI imaging capability of ultrasmall Mn_3O_4 nanoparticles for tumors, the liver metastatic tumor was applied to perform the evaluation. MRI imaging results after the construction of the liver metastatic tumor model and the intravenous injection of Mn_3O_4 (5 mg kg^{-1}) are shown in Fig. 7a. The lightness in the liver part shows graininess, and the intensity is significantly enhanced (inside the white circle). Compared with the PBS group, the signal intensity increases 159.7%, which conveys effective MRI detection ability for the metastatic tumor. The real image of the liver metastatic tumor (Fig. 7b) and the corresponding histological tissue sections of the liver and liver metastatic tumor (Fig. 7c) are consistent with the MRI image results, thus positioning ultrasmall Mn_3O_4 nanoparticles as a promising candidate for overcoming the obstacle of accurate diagnosis for tumor metastasis.

3.4 Biosafety assessment of ultrasmall Mn_3O_4 nanoparticles

The *in vivo* biosafety of ultrasmall Mn_3O_4 nanoparticles is evaluated using the hemolysis ratio and HE staining of main

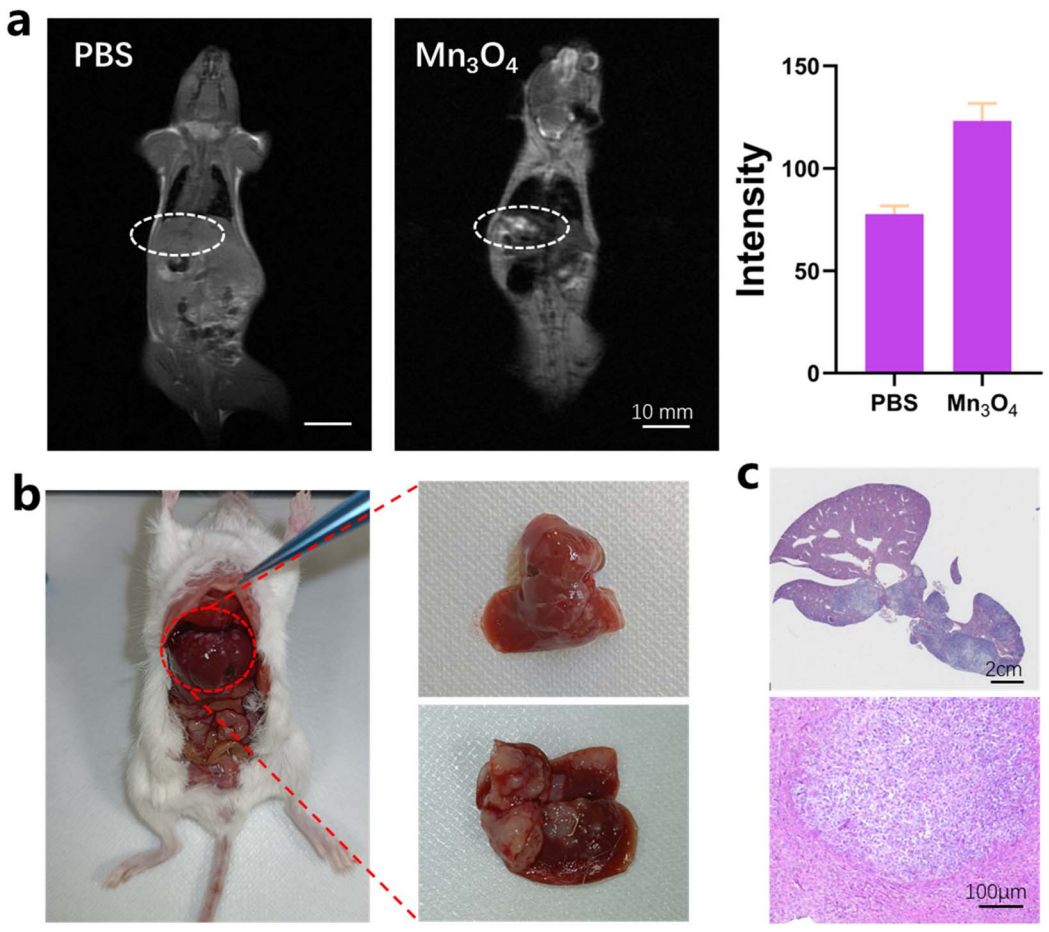

Fig. 7 MRI imaging, real image and tissue slicing staining of the liver metastatic tumor. (a) MRI imaging of the liver metastatic tumor and intensity statistic. (b) The real image of the liver metastatic tumor and (c) the corresponding histological tissue sections staining of the liver and metastatic tumor.

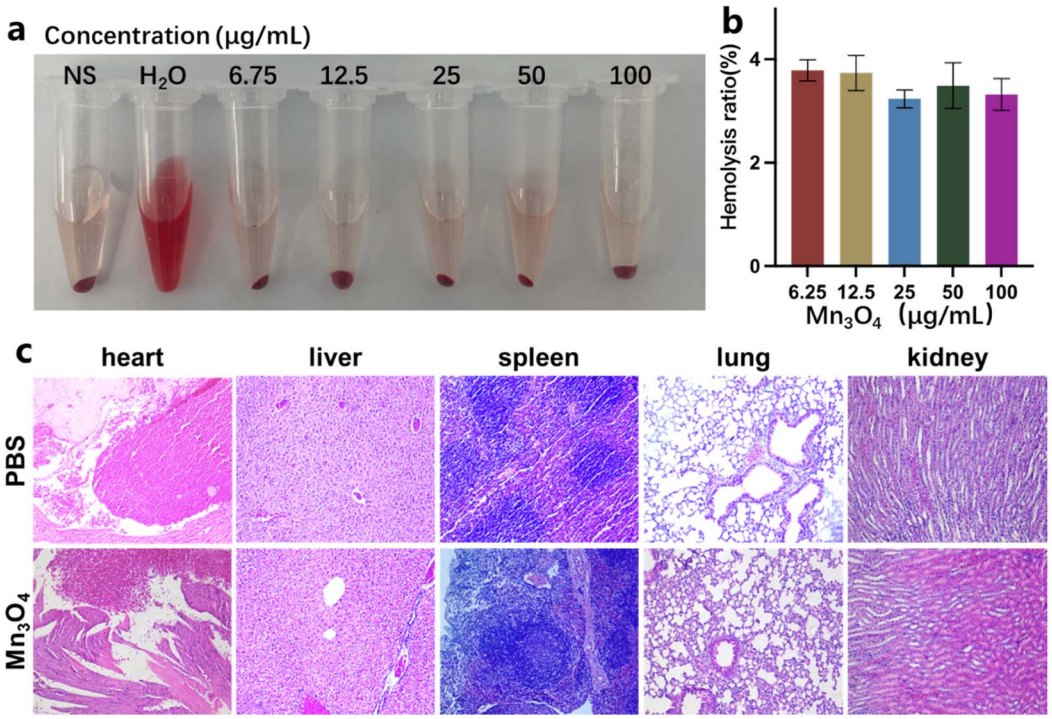

Fig. 8 Biosafety assessment of ultrasmall Mn_3O_4 nanoparticles. (a) The real image of the hemolysis experiment and (b) hemolysis ratio. (c) HE staining of histological tissue sections of major organs after injecting Mn_3O_4 nanoparticles.

organs. The hemolysis ratio (Fig. 8a and b) of Mn_3O_4 nanoparticles (6.25, 12.5, 25, 50, and 100 μg mL^{-1}) remains smaller than 4%, revealing a good hemocompatibility for *in vivo* application. As shown in Fig. 8c, after treatment with Mn_3O_4 nanoparticles *in vivo*, the sections from the main organ and tissues have no histological difference compared with the PBS group. Moreover, no histopathological damage, including necrosis and inflammatory response, is observed. These biosafety results demonstrate that the designed ultrasmall Mn_3O_4 nanoparticles possess excellent biocompatibility *in vivo* and could be used for further biomedical applications.

4. Conclusion

In summary, an effective and novel design of ultrasmall Mn_3O_4 nanoparticles with an integrated multifunction is proposed. Ultrasmall Mn_3O_4 nanoparticles with excellent uniformity and stability could be produced on a large scale. The designed Mn_3O_4 nanoparticles could react and be decomposed by GSH owing to the existence of high valence Mn in the nanocrystals, which endow the responsive capability in the tumor microenvironment. Moreover, the GSH-responsive property enable Mn_3O_4 with the T_1 turn-off and T_2 turn-on MRI imaging variation effects and effectively enhance the imaging intensity and quality. The unique T_1/T_2 MRI imaging could be applied to subcutaneous tumors and liver metastases tumors for promoting accurate tumor diagnosis. Moreover, the ultrasmall Mn_3O_4 nanoparticles possess an excellent ferroptosis therapy effect toward tumor cells, which presents superb prospects for tumor treatment. The well-designed integrated multifunction in individual ultrasmall Mn_3O_4 nanoparticles demonstrates an innovative strategy for effective tumor treatment under MRI guidance and holds considerable potential for cancer treatment in the clinic.

Data availability

Data will be made available upon reasonable request.

Author contributions

Q. H. X. and J. Z. D completed most of the experiments and manuscript. G. R. Z. and D. W. Z. performed partial experiments, including the MRI test and cell staining. H. L. and D. X Y. provided careful guidance and adequate experimental support for this work.

Conflicts of interest

The authors declare no known competing financial interests or personal relationships.

Acknowledgements

This work was supported by the Key Research and Development Program of Shandong Province (2021CXGC010603) and Shandong Provincial Natural Science Foundation (ZR2023QE146). National Key Research and Development Program of China (2023YFB3210400)

References

1 Q. He, H. Hu, Q. Zhang, T. Wu, Y. Zhang, K. Li, *et al.*, *Chem. Eng. J.*, 2020, **397**, 125478.
2 G. Yang, L. Xu, Y. Chao, J. Xu, X. Sun, Y. Wu, *et al.*, *Nat. Commun.*, 2017, **8**(1), 902.
3 W. Yang, C. Xiang, Y. Xu, S. Chen, W. Zeng, K. Liu, *et al.*, *Biomaterials*, 2020, **255**, 120186.
4 H. B. Na, J. H. Lee, K. An, Y. I. Park, M. Park, I. S. Lee, *et al.*, *Angew. Chem., Int. Ed.*, 2007, **46**(28), 5397–5401.
5 T.-H. Shin, P. K. Kim, S. Kang, J. Cheong, S. Kim, Y. Lim, *et al.*, *Nat. Biomed. Eng.*, 2021, **5**(3), 252–263.
6 Y. Luo, J. Yang, J. Li, Z. Yu, G. Zhang, X. Shi, *et al.*, *Colloids Surf., B*, 2015, **136**, 506–513.
7 B. H. Kim, N. Lee, H. Kim, K. An, Y. I. Park, Y. Choi, *et al.*, *J. Am. Chem. Soc.*, 2011, **133**(32), 12624–12631.
8 S. Zhao, J. Duan, Y. Lou, R. Gao, S. Yang, P. Wang, *et al.*, *Nanoscale*, 2021, **13**(45), 19109–19122.
9 Q. Xie, X. Wang, G. Zhang, D. Zhou, Y. Zhao, H. Liu, *et al.*, *Sci. Rep.*, 2024, **14**(1), 10646.
10 Q. Jia, J. Ge, W. Liu, X. Zheng, S. Chen, Y. Wen, *et al.*, *Adv. Mater.*, 2018, **30**(13), 1706090.
11 D. Wang, H. Wu, W. Q. Lim, S. Z. F. Phua, P. Xu, Q. Chen, *et al.*, *Adv. Mater.*, 2019, **31**(27), 1901893.
12 L. Gao, Y. Zhang, L. Zhao, W. Niu, Y. Tang, F. Gao, *et al.*, *Sci. Adv.*, 2020, **6**(29), eabb1421.
13 L. Feng, B. Liu, R. Xie, D. Wang, C. Qian, W. Zhou, *et al.*, *Adv. Funct. Mater.*, 2020, **31**(5), 2006216.
14 S. I. Han, Sw Lee, M. G. Cho, J. M. Yoo, M. H. Oh, B. Jeong, *et al.*, *Adv. Mater.*, 2020, **32**(31), 2001566.
15 Y. Chen, Q. Yin, X. Ji, S. Zhang, H. Chen, Y. Zheng, *et al.*, *Biomaterials*, 2012, **33**(29), 7126–7137.
16 J. Xiao, X. M. Tian, C. Yang, P. Liu, N. Q. Luo, Y. Liang, *et al.*, *Sci. Rep.*, 2013, **3**(1), 2045.
17 R. Wei, X. Gong, H. Lin, K. Zhang, A. Li, K. Liu, *et al.*, *Nano Lett.*, 2019, **19**(8), 5394–5402.
18 Z. Yi, Z. Luo, N. D. Barth, X. Meng, H. Liu, W. Bu, *et al.*, *Adv. Mater.*, 2019, **31**(37), 1901851.
19 X. Li, S. Lu, Z. Xiong, Y. Hu, D. Ma, W. Lou, *et al.*, *Adv. Sci.*, 2019, **6**(19), 1901800.
20 S. Bai, N. Yang, X. Wang, F. Gong, Z. Dong, Y. Gong, *et al.*, *ACS Nano*, 2020, **14**(11), 15119–15130.
21 X. Xu, X. Zhou, B. Xiao, H. Xu, D. Hu, Y. Qian, *et al.*, *Nano Lett.*, 2021, **21**(5), 2199–2206.
22 J. Shi, W. Yu, L. Xu, N. Yin, W. Liu, K. Zhang, *et al.*, *Nano Lett.*, 2019, **20**(1), 780–789.
23 H. J. Kwon, K. Shin, M. Soh, H. Chang, J. Kim, J. Lee, *et al.*, *Adv. Mater.*, 2018, **30**(42), 1704290.
24 B. Ding, P. Zheng, Pa Ma and J. Lin, *Adv. Mater.*, 2020, **32**(10), 1905823.
25 Y. Zhan, S. Shi, E. B. Ehlerding, S. A. Graves, S. Goel, J. W. Engle, *et al.*, *ACS Appl. Mater. Interfaces*, 2017, **9**(44), 38304–38312.
26 J. Duan, S. Zhao, Y. Duan, D. Sun, G. Zhang, D. Yu, *et al.*, *Adv. Healthc. Mater.*, 2024, 2303963.
27 N. Singh, M. A. Savanur, S. Srivastava, P. D'Silva and G. Mugesh, *Angew. Chem., Int. Ed.*, 2017, **129**(45), 14455–14459.
28 Y. Liu, J. Yang, B. Liu, W. Cao, J. Zhang, Y. Yang, *et al.*, *Nano-Micro Lett.*, 2020, **12**(1), 127.
29 X. Zeng, S. Yan, P. Chen, W. Du and B.-F. Liu, *Nano Res.*, 2020, **13**(6), 1527–1535.
30 W. Wang, J. Duan, W. Ma, B. Xia, F. Liu, Y. Kong, *et al.*, *Adv. Sci.*, 2023, **10**(17), 2205859.